WaveComBE

mmWave Communications in the Built Environments

WaveComBE_D3.2

Report on the optimization of mmW MIMO configurations for small cells in the built environments

Version Final Date: 31/03/2021

Document properties:

Grant Number:	766231
Document Number:	D3.2
Document Title:	Report on the optimization of mmW MIMO configurations for small cells in the built environments
Partners involved:	USFD, UDUR, UT, LTV, RPN, UPV
Authors:	Yixin Zhang, Chen Chen, Danaisy Prado-Alvarez, Monika Drozdowska, Chunxia Qin, Narcís Cardona, Jose F. Monserrat, Frederik Naessens, Xiaoli Chu, Jie Zhang
Contractual Date of Delivery:	2021/03/31
Dissemination level:	PU[1]
Version:	Final
File Name:	WaveComBE D3.2

[1] CO = Confidential, only members of the consortium (including the Commission Services)

PU = Public

Table of contents

Executive Summary

The large available bandwidth at millimeter wave (mmW) frequencies makes them attractive for the fifth generation (5G) of mobile networks. In this deliverable, we investigate how to optimize the MIMO configurations for mmW small cells, how to optimize the MIMO configurations for high-date-rate conferencing scenarios, and how to design the signal processing solutions for mmW massive MIMO.

The existing works have mostly considered a 2D network model, ignoring the heights of base stations (BSs) and user equipment (UEs). In Chapter 2, we present a new three-dimensional (3D) mmW small cell (SC) model using the tools from stochastic geometry. More specifically, we assume that the locations of BSs, UEs and blockages follow three independent Poisson point processes. We model both the antenna downtilt gain for a single directional BS antenna and the analog beamforming gain for the BS antenna array. Then, we derive the 3D Line-of-Sight (LOS) probability from a BS to a UE and the area spectral efficiency (ASE) of the SC network. The numerical results show that the ASE first increases linearly and then decreases with the BS density and that a lower BS height and a larger BS antenna downtilt lead to a larger maximum achievable ASE.

In Chapter 3, we describe the indoor built environments (BE) setups and model the wireless channel in the mmW band considering the effects of wall reflection (WR) and diffuse scattering (DS). The dimensions of example conference rooms and offices, the typical conference room setups, and the building material properties are presented. We identify the challenges that have to be overcome, and the requirements for video conferencing as a high-data-rate service. The techniques related to multi-user (MU) grouping, centralized multiple-input multiple-output (MIMO), and antenna selection based on distributed MIMO are introduced. Numerical results show that the highly correlated UEs should be served separately through the user grouping technique, and that antenna selection based on distributed subarray configurations can enhance the sum rate when serving multiple UEs simultaneously.

In Chapter 4, in order to overcome the body blockage effects, we develop solutions based on distributed antenna system (DAS). One of such solutions is ubiquitous cell-free massive MIMO, which consists of a large number of access points (APs) that coherently serve a much smaller number of UEs, where there are no cell boundaries among the APs. More specifically, we evaluate the impact of body blockage on the performance of cell-free mmW Massive MIMO systems in terms of spectral efficiency in indoor environments, while considering different densities of APs and UEs for the same total number of antennas and the same radiated power. For the sake of fairness in the resource allocation, a max-min fairness (MMF) optimization is applied in the design of digital precoders.

Disclaimer: This work has been performed in the framework of the H2020 project WaveComBE (Grant agreement ID: 766231) co-funded by the EU. This information reflects the consortium's view, but the consortium is not liable for any use that may be made of any of the information contained therein. This deliverable has been submitted to the EU commission, but it has not been reviewed and it has not been accepted by the EU commission yet.

List of Figures

List of Tables

List of Acronyms and Abbreviations

2D	Two-dimensional
3D	Three-dimensional
5G	Fifth Generation
AP	Access Point
AR	Aspect Ratio
ASE	Area Spectral Efficiency
AWGN	Additive White Gaussian Noise
BE	Built Environment
BS	Base Station
CPU	Central Processing Unit
CSI	Channel State Information
DAR	3D Room Diagonal divided by AR
DAS	Distributed Antenna System
DS	Diffuse Scattering
EM	Electromagnetic
GS	Group Selection
HPBW	Half-Power Beamwidth
LOS	Line-Of-Sight
MAC	Medium Access Control
MIMO	Multiple Input Multiple Output
MMF	Max-Min Fairness
mmW	Millimeter Wave
MRT	Maximum Radio Transmission
MU-MIMO	Multi User MIMO
OFDMA	Orthogonal Frequency Division Multiple Access
PHY	Physical Layer
PPP	Poisson Point Process
QoS	Quality of Service
RF	Radio Frequency

RMS DS	Root Mean Square Delay Spread
RS	Random Selection
SC	Small Cell
SE	Spectral Efficiency
SHF	Super High Frequency
SINR	Signal-to- Interference-plus-Noise Ratio
STA	Station
SU-MIMO	Single User MIMO
TDD	Time Division Duplexing
TE	Transverse Electric
TM	Transverse Magnetic
WM	Wireless Medium
WR	Wall Reflection

1. Introduction

Although the previous generations of mobile technologies have mainly focused on satisfying human-to-human communications, this is no longer enough - we are experiencing a global digital transformation! In this context, 5G emerges with a bunch of promising solutions to effectively connect all kinds of things that surround us such as vehicles, machines, and of course, ourselves. To meet the challenging goals of the 5G, new cutting-edge technologies are needed. In this sense, the millimeter wave (mmW) band has been selected as a 5G enabler, due to the huge available bandwidths at mmW frequencies.

The mmW band contains a wide range of carrier frequencies and large bandwidths capable of supporting short-range high-rate wireless connectivity. The mmW band has several distinct features including compatibility with directional transmissions, reasonable isolation, and dense deployability [1]. Thanks to the small wavelength, it is possible to pack multiple antenna elements into the limited space at mmW transceivers. With large antenna arrays, mmW cellular systems can implement beamforming at the transmitter and receiver to provide a large array gain that compensates for the frequency-dependent path loss, overcomes additional noise power, and as a bonus also reduces out-of-cell interference.

In addition, mmW signals are more sensitive to blockage effects than signals in lower-frequency bands, as certain materials such as concrete walls found on building exteriors cause severe penetration losses [2]. The distinct effects of the blockages need to be incorporated into the comprehensive system analysis of mmW networks.

Dense deployment of small cell networks (SCN) is considered as one of the key techniques of 5G networks [3]. The traditional understanding of network densification is that the increase of BS density does not change the coverage probability of the typical UE in an interference limiting scenario [4], [5]. This indicates that the area spectral efficiency (ASE) scales linearly with the BS density, and thus the capacity gain can always be obtained. However, it is worth noting that this result is based on the simplified free space propagation channel model. Considering the short-range propagation in dense SCNs, the authors in [6], [7] proposed a bounded path loss model and showed that the ultra-dense network degrades the spatial throughput. In [8], a multi-slope path loss model was employed to study the effect of non-line-of-sight transmission on the coverage probability. Their results showed that when the BS density increases above a certain value, the coverage probability starts to decrease and the increase of ASE slows down. In [9], the authors studied the effect of the height of BS antennas on the coverage probability and the ASE, which decrease to zero with the BS density when the BSs are higher than the UEs.

To meet the high data demand and address the capacity crunch, small base stations (BSs) are usually equipped with large-scale MIMO antenna arrays, e.g. consisting of hundreds of antennas. Transmission in the mmW bands lessens the antenna size and thus makes large-scale multiple-input multiple-output (MIMO) techniques achievable at the transceivers [10-12].

Spatial multiplexing and beamforming are two key techniques in MIMO. Spatial multiplexing provides multiplexing gain by subdividing an outgoing signal stream into multiple pieces. Beamforming offers high directional antenna gain where multiple antenna elements are adaptively phased to form a concentrated and directed beam pattern. The authors in [11] proposed an mmW MIMO architecture, which utilizes arrays of subarrays to provide both directivity and spatial multiplexing gains. The results showed that this architecture can provide

the spatial multiplexing gain robust to LOS blockage and to variations in the locations of the transmitter and receiver within the room. According to the experimental results of mmW MIMO prototypes in [12] that confirms the negative impact of hand/human blockages and material penetration losses on the link margins, it is necessary to reap spatial array gains by using near-optimal beamformers over large-scale antenna arrays.

Despite of the wide bandwidth spectrum offered by the mmW band, the high path-loss and severe shadow fading inherent to the super high frequency (SHF) band are challenging. This fact opens new branches in the study of wireless propagation, where the possibility of designing versatile antennas with several elements arises as the most evident way forward to compensate for such losses. An extreme case for this solution is massive MIMO in which very large antenna arrays are used at BS to simultaneously serve several users. Following this line and considering such amount of antenna elements the question about using architectures based on compact arrays or distributed antenna systems emerged [13]. In [13], cell-free massive MIMO [14] was proposed as one of the solutions for a massive MIMO system geographically distributed. These systems form a promising solution to overcome, for example, the effects of the blockage since antennas are everywhere so the users can be surrounded by them.

In [15], the authors proposed and validated experimentally the channel models that consider body blockage for an office scenario, and they stressed that it should be possible to reach high-density deployments if a ceiling-mounted AP with very narrow beams was used. However, the analysis of the densification limits is still an open problem. In [16], the evaluation of the suitability of cell-free massive MIMO to counteract the body blockage in indoor scenarios was only discussed as part of future work.

One of the mainstays of massive MIMO mmW systems is the signal steering in narrow beams to concentrate most of the power in a given direction. That said, beamforming techniques are essential at mmW frequencies. In order to guarantee a high level of flexibility in the generation of the beams, a fully digital precoders architecture is adopted.

The tool of stochastic geometry has been widely used to study the performance of mmW wireless networks due to its tractability and accuracy. In [2], an equivalent LOS ball model was proposed to approximate the effect of blockages and a sectorized model was used to simplify the analysis of beamforming gain. However, this work only considered a two-dimensional (2D) network deployment. In [17], the blockages were modelled as cylinders and the 3D antenna gain was characterized. The system-level metrics such as coverage probability and area spectral efficiency (ASE), however, were not analyzed. As aforementioned, the performance of a three-dimensional (3D) mmW network needs to be evaluated considering the effects of blockages and antenna array gain in 3D space.

To fill in the above identified gaps in the existing works, this report focuses on jointly optimizing massive MIMO configurations and Radio Frequency (RF) properties of BEs for mmW SC deployment, which will be detailed in the following chapters.

- In Chapter 2, a general analytical framework for a 3D mmW SC network based on tools from stochastic geometry is proposed. The BS directional beamforming and a 3D blockage model have been incorporated in the analysis. The relationship between the ASE and the BS height as well as BS density is revealed.
- In Chapter 3, the mmW massive MIMO configurations, the environment properties and their influence on the mmW signal propagation are described, as well as the technical

requirements for high-data-rate audio and video conferencing services. Based on these models and requirements, the techniques related to multi-user grouping, centralized MIMO, and antenna selection are provided.

- In Chapter 4, a fully digital architecture is proposed to evaluate the deployment densification limits and the impact of the body blockage on the spectral efficiency of an mmW SC network in an industrial warehouse scenario. The dependence between the body blockage probability and the densities of APs and UEs is revealed and analyzed.
- The report is concluded in Chapter 5.

2. Optimizing MIMO configurations for mmW small cells

2.1. System model

2.1.1. Network and channel models

We propose a novel 3D mmW SC network model using stochastic geometry, where the base stations (BSs), user equipment (UEs) and blockages are distributed according to three 2D homogeneous Poisson point processes (PPP) with intensities λ_{B}, λ_{b} and λ_{u}, respectively. The BS height is a constant H_{B} and the UE height is a constant H_{u}. The blockage height is H_{b} following an exponential distribution with the parameter ω. The line Boolean model [18] is used to model the blockages, where the length and orientation are both uniformly distributed with mean values L and π, respectively. We assume that orthogonal time/frequency resource partitioning is adopted, e.g., orthogonal frequency division multiple access (OFDMA).

We consider a wireless channel that is characterized by both large-scale and small-scale fading. The large-scale fading is the path loss between a BS and a UE. For small-scale fading, we adopt a Nakagami-m model [19] for the channel gain, where fading parameter m is assumed to be an integer for tractability. The channel gain power is a Gamma random variable $g \sim \Gamma(m,\ 1/m)$.

2.1.2. 3D BS antenna pattern

We assume that each UE is equipped with an isotropic antenna and each BS is equipped with a planar square array comprising N directional antennas of fixed radiation patterns. The total antenna gain is the product of the directional antenna gain and antenna array gain. For our SC BSs, we adopt the dipole antenna pattern [20], which is expressed in linear scale by

$$G(\theta) = G_{\mathrm{H}} G_{\mathrm{V}} G_{\mathrm{M}}, \tag{2-1}$$

where θ is the elevation angle of a BS, $G_{\mathrm{H}} = 0$ dB is the directional antenna gain in the horizontal dimension, $G_{\mathrm{V}} = \max\{\cos^{p}(\theta - \gamma),\ T_{\mathrm{v}}\}$ is the directional antenna gain in the vertical dimension, where γ is the electrical antenna downtilt and T_{v} is the side lobe level, and G_{M} is the maximum antenna gain.

The actual antenna array pattern is a function of the azimuth angle and the elevation angle from the serving BS to the UE. For simplicity, we use the 3D sectorized antenna array model [1], which is a function of the half-power beamwidth (HPBW) in the horizontal dimension ϑ_{H} and that in the vertical dimension ϑ_{V}. The array gain is either main-lobe gain G_{main} or side-lobe gain G_{side}. The main-lobe gain can be obtained with probability 1 at a UE from its serving BS, while from its interfering BS, the probability of receiving main-lobe gain is P_{main} and the probability of receiving side-lobe gain is P_{side}. The expressions of ϑ_{H}, ϑ_{V}, G_{main}, G_{side}, P_{main} and P_{side} can be found in [18].

2.1.3. LoS probability

We analyze the Line-Of-Sight (LOS) probability from a BS to a UE with a horizontal link length r. According to [19], the horizontal LOS probability can be derived as $e^{-\beta r}$, where $\beta = 2\lambda_{\mathrm{b}} L/\pi$. Then the 3D LOS probability is computed by $e^{-\xi\beta r}$, where $\xi = \frac{e^{-\omega H_{\mathrm{u}}} - e^{-\omega H_{\mathrm{B}}}}{\omega(H_{\mathrm{B}} - H_{\mathrm{u}})}$.

2.2. Performance analysis

2.2.1. Area spectral efficiency

In this subsection, we analyze the ASE of the mmW SC network, which is defined as the average spectral efficiency of a unit area. We assume that the penetration loss of the blockages goes to infinity [21] and each UE is connected to its nearest LOS BS. Under this assumption, the ASE is given by [22]

$$ASE = \lambda_{\mathrm{B}} \log_2(1+\eta) P_{\mathrm{coverage}}, \tag{2-2}$$

where η is the signal-to-noise-plus-interference ratio (SINR) threshold and P_{coverage} is the coverage probability given by

$$P_{\mathrm{coverage}} \approx \sum_k^m (-1)^{k+1} \binom{m}{k} \int_0^\infty e^{-2\pi\lambda_{\mathrm{B}} \int_y^\infty O(y,v) e^{-\xi\beta v} v \mathrm{d}v - \frac{\epsilon k \eta}{\mathrm{SNR}(y)}} f(y) \mathrm{d}y\,, \tag{2-3}$$

where $\epsilon = m(m!)^{-1/m}$, $\mathrm{SNR}(y) = q(y) G_{\mathrm{V}}(y)/\rho$, $q(y) = \sigma(y^2 + (H_{\mathrm{B}} - H_{\mathrm{u}})^2)^{-\alpha/2}$, α is the path loss exponent, σ is the path loss at the reference distance, $\rho = \chi/(P G_{\mathrm{main}} G_{\mathrm{M}})$, where χ is the additive white Gaussian noise (AWGN) power, P is the transmission power of BSs, $G_{\mathrm{V}}(y) = \max\{\cos^p\left(\arctan(\frac{H_{\mathrm{B}} - H_{\mathrm{u}}}{y}) - \gamma\right), T_{\mathrm{v}}\}$, $O(y,v) = 1 - [1 + \frac{k\epsilon\eta G_{\mathrm{I}} G_{\mathrm{V}}(v) q(v)}{m G_{\mathrm{V}}(y) q(y)}]^{-m}$, $G_{\mathrm{I}} = (G_{\mathrm{main}} P_{\mathrm{main}} + G_{\mathrm{side}} P_{\mathrm{side}})/ G_{\mathrm{main}}$, $f(y) = 2\pi\lambda_{\mathrm{B}} y e^{-2\pi\lambda_{\mathrm{B}} Z(y) - \xi\beta y}$, $Z(y) = \frac{1 - e^{-\xi\beta y}(1+\xi\beta y)}{(\xi\beta)^2}$.

2.3. Simulation results

In this subsection we show the simulation results and analyze the effects of BS height and antenna downtilt on the ASE. The default parameters for our simulation are given in Table 2-1.

Table 2-1. The default parameters for simulations

Parameter	Value
Path loss exponent: α	2
AWGN power: χ	-74 dBm
Transmission power: P	33 dBm
Threshold of SINR: η	10 dB
BS intensity: λ_{B}	0.01 BS/m^2
Blockage intensity: λ_{b}	0.05 blockage/m^2
BS height: H_{B}, UE height: H_{u}	3 m, 1m
Antenna number per array: N	36
Blockage parameters: L, ω	2 m, 3/2
Antenna downtilt: γ	30°
Parameter of small scale fading: m	3

2.3.1. Effect of BS height

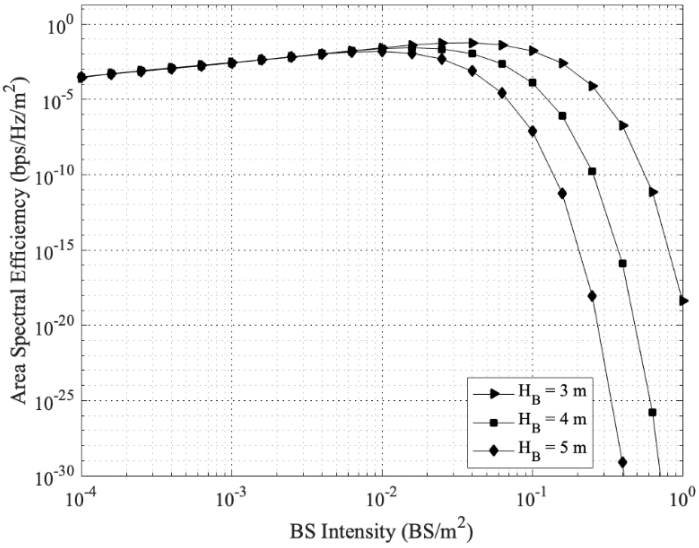

Fig. 2-1. ASE versus BS intensity for different BS height

In Fig. 2-1, we plot the ASE versus λ_B for different BS heights. As can be seen, the ASE first increases linearly with λ_B, and then decays towards zero when the network becomes ultra-dense. The maximum ASE achievable decreases with the increase of H_B, indicating that the BS height should be lower for the deployment of ultra-dense SC networks.

2.3.2. Effect of antenna downtilt

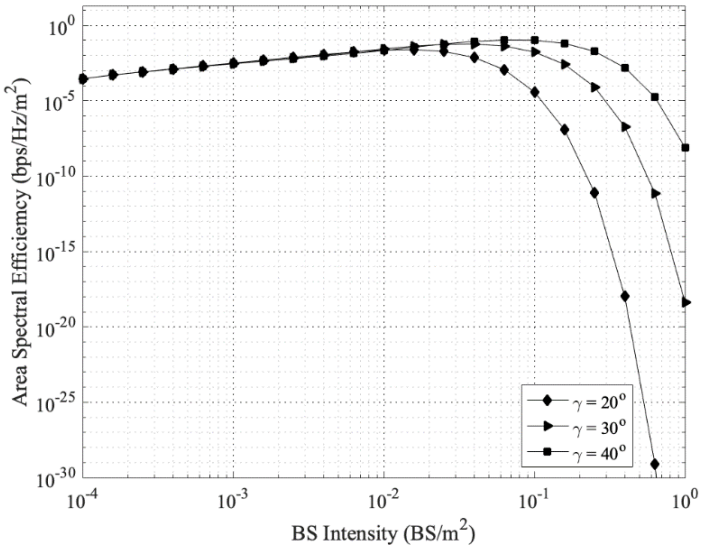

Fig. 2-2. ASE versus BS intensity for different antenna downtilt

In Fig. 2-2, we plot the ASE versus λ_B for different antenna downtilts. Similar with the trend in Fig. 2-1, the ASE first increases linearly with λ_B, and then decays towards zero when the network becomes ultra-dense. The maximum ASE achievable monotonically increases with the increase of γ, indicating that a large antenna downtilt is preferable for the deployment of ultra-dense SC networks.

3. Optimizing mmW MIMO configurations for high-data-rate conferencing services

3.1. Modelling for offices and large conference rooms

Plenty of aspects must be taken into account when we are optimizing mmW massive multiple-input multiple-output (MIMO) configurations. First, we need to define the environment. Its destination, geometrical properties, materials used to build walls and furniture. The setup of the furniture, number of participants, the sources of possible signal blockage, restricted places where we can't put antennas, etc. In this section, we will make a detailed summary of those properties for offices and conference rooms.

For the conference use case it is important to define used terminology:

- Access Point (AP) - networking hardware device that allows other Wi-Fi devices to connect to a wired network.
- User Equipment (UE) - a station (STA) defined in IEEE 802.11 group of standards as a logical entity that is a singly addressable instance of a medium access control (MAC) and physical layer (PHY) interface to the wireless medium (WM) with additional facilities like screen, video camera, microphone, and/or listening facilities (headphones, loudspeaker),
- President - leader of the meeting,
- Chairman - co-leader in a panel or forum,
- Participants - delegates participating into the discussion (equipped in UEs with microphone and listening facilities),
- Listeners - people in the room with only listening facilities.

3.1.1. Venue size and shape

Geometrical properties of the environment are independent from radio frequency, but may depend on the shape. We always can define:

- Height (H [m]),
- Surface area [m^2],
- Volume [m^3].

According to the floor plan, we can distinguish rooms that are square, rectangular, parallelogram, polygonal, triangular, trapezoidal, circle, or ellipsoidal.

According to the volume, we can distinguish rooms that are cubical, cuboidal, spherical, ellipsoidal, cylindrical, conical, pyramidal, or torus.

The most common rooms have square or rectangular floor plans and cubical or cuboidal volume. For them we can additionally define:

- Walls' lengths (L [m], W [m]),
- 3D Diagonal (d_{3D} [m]),
- AR [-],
- DAR [m].

It is ambiguous to call the room small or large if only two dimensions (*L* and *W*) are taken into account. Especially when we need to characterize the environment for the radio waves propagation, where important is the distance between transmitter and receiver and also their distance to the walls, ceiling and floor. Besides, environments with the same diagonal, area or volume may have different aspect ratio, which may have a great impact on the reflected waves. This is why next to standard parameters the DAR value was introduced for rectangular rooms.

$$DAR\ [\mathrm{m}] = d_{3D}\ [\mathrm{m}] \,/\, AR \tag{3-1}$$

A large value of DAR indicates rooms with large dimensions and small AR (large square rooms). For a square room, the decreasing of the DAR value means lowering the ceiling or shortening the walls. The decrease of the DAR may also be the consequence of the AR increasing. For rooms with the same volume, surface, or diagonal, but different AR, DAR will be smaller for longer and narrower environments.

Table 3-1. Example office and conference rooms

ENV. TYPE	d3D [m]	Area [m^2]	Volume [m^3]	AR	DAR [m]	DIMENSIONS [m x m x m]	REF.
Small conference room	7.72	20.92	51.89	2.07	3.73	6.6 x 3.2 x 2.5	[23]
Small conference room	6.18	13.5	40.50	1.5	4.12	4.5 x 3 x 3	[24]
Small conference room	10.88	50.16	145.46	1.54	7.04	8.8 x 5.7 x 2.9	[25]
Conference room	9.91	39.53	169.98	1.14	8.72	6.7 x 5.9 x 4.3	[26]
Conference room	15.87	105.98	275.55	1.74	9.13	13.57 x 7.81 x 2.6	[27]
Office	5.2-5.66	11.25	22.5-33.75	1.25	4.16-4.5	3.75 x 3 x (2-3)	[28]
Office	10.62	51.84	155.52	1	10.61	7.2 x 7.2 x 3	[29]
Open-space office	13.81	89.01	275.93	1.2	11.43	10.35 x 8.6 x 3.1	[30]
Office	15.09	110	286	1.1	13.72	11 x 10 x 2.6	[31]

Some of the office and conference room environments, for which RMS DS in 60 GHz band measurements results were reported in the literature, are listed in Table 3-1 above together with their dimensions. All of them are cuboidal. Except for the square office from [29] and polygonal open-space office from [30], all have rectangular floor plans.

Note that mentioned conference rooms are in majority small or regular size (except the one from [27] that can be considered large). Examples of large conference rooms in various shapes, are listed below.

Large conference rooms:

- *L* = 16 m - 19 m
- *W* = 10 m - 11 m
- Number of participants: 30 - 45

Very large conference rooms:

- *L* = 22.5 m - 35 m
- *W* = 14.5 m - 16 m
- Number of participants: 120 - 280

3.1.2. Typical building materials

Traditional building materials that are commonly used in constructions include: concrete, brick, plasterboard, wood, glass [32]. The concrete and brick walls are typical structures in building facades and between rooms [33-36]. Plasterboards are often used as interior walls to separate two rooms [36,37]. Glass and wood can be manufactured for windows, doors and partitioners [38-40].

It has been shown that the dielectric property of a building material is dependent on the proportion among different chemical components [33] as well as the surrounding humidity [35]. The advantages of traditional materials are cheap price, readily available raw materials, and simple production method, which makes them widely applied in constructions.

The interactions between the building materials and the incident electromagnetic (EM) waves should be effectively characterized. EM waves emitted from the transmitter often experience complicated processes, e.g., one-bounce reflection, two-bounce reflection, diffuse scattering, with the interacting physical objects before arriving at the receiver. Meanwhile, indoor built environments differ widely in the materials used for walls, ceilings and floors, windows, obstructing objects. The variation of the EM and physical properties of building materials will bring great changes in the wireless network performance [41,42]. As stated in [43], the reflection characteristics of common building materials will be required for the planning and design of future wireless communication systems.

Specifically, a wall can be regarded as a lossy dielectric structure [44]. An EM wave would suffer reflection loss after hitting on the wall's surface due to multiple internal reflections, as shown in Fig. 3-1. Measurement results have shown that the reflection loss is dependent on the incident angles and polarisation of EM waves, and the physical (thickness) and EM properties (relative permittivity) of wall materials [45], which is mathematically characterised by the Fresnel equations [46].

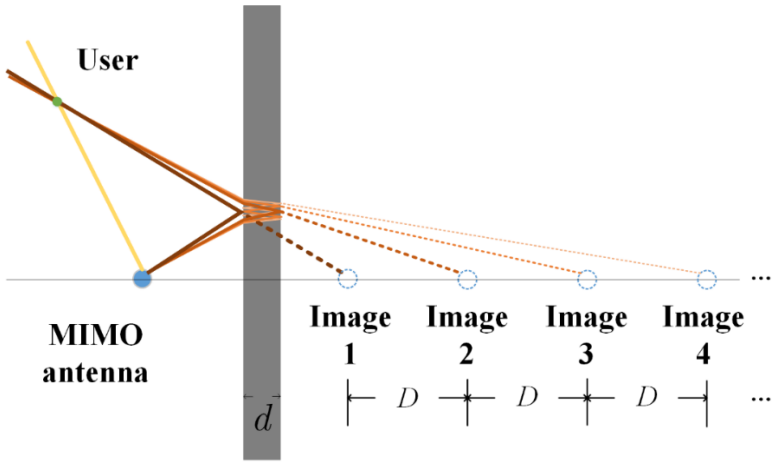

Fig. 3-1. Multiple internal reflections inside the wall material

A simple approach to describing the relative permittivity is provided in [46], which is given by

$$\varepsilon = \varepsilon_0 - j\varepsilon_1, \tag{3-2}$$

where the real part and the imaginary part can be expressed as a function of frequency f, respectively, i.e.,

$$\varepsilon_0 = uf^v, \tag{3-3}$$

$$\varepsilon_1 = 17.98\sigma/f, \tag{3-4}$$

where $\sigma = rf^t$ is the conductivity of the building material, and constants u, v, r and t are compiled in [46, Table. 2].

Supposing that the wall is a single-layer reflector, the multiple internal reflections inside it are strongly affected by the first-order reflection. The first-order reflection coefficient Γ' for the incident electric field of transverse electric (TE) polarisation Γ_{TE} and transverse magnetic (TM) polarisation Γ_{TM} are given respectively by

$$\Gamma_{\mathrm{TE}} = \frac{\cos\alpha - \sqrt{\varepsilon - \sin^2\alpha}}{\cos\alpha + \sqrt{\varepsilon - \sin^2\alpha}}, \tag{3-5}$$

or

$$\Gamma_{\mathrm{TM}} = \frac{\cos\alpha - \sqrt{(\varepsilon - \sin^2\alpha)/\varepsilon^2}}{\cos\alpha + \sqrt{(\varepsilon - \sin^2\alpha)/\varepsilon^2}}, \tag{3-6}$$

where α denotes the incident angle and ε denotes the relative permittivity of the building material.

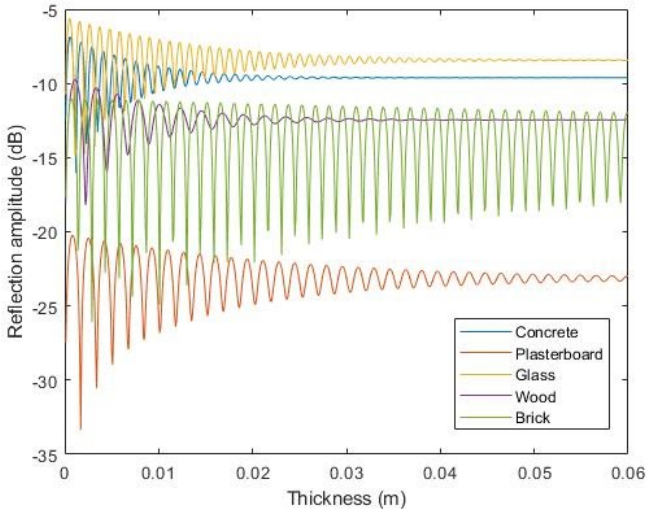

Fig. 3-2. The multiple reflection coefficient amplitudes of five different materials for the TM polarised 60-degree incident wave under 60 GHz

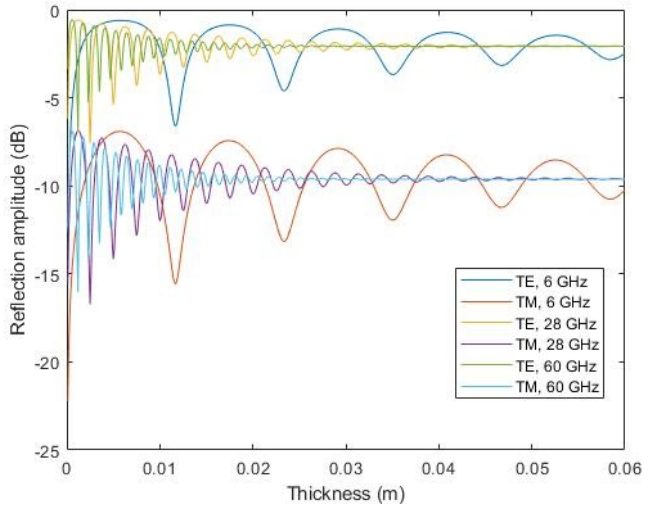

Fig. 3-3. The multiple reflection coefficient amplitudes of a concrete material for the TE and TM polarised 60-degree incident wave under 6 GHz, 28 GHz, 60 GHz.

In Fig. 3-2, the multiple reflection coefficient amplitudes of five different materials for the TM polarised 60-degree incident wave under 6 GHz are depicted. The five materials are shown to have their inherent reflection characteristics.

Fig. 3-3 plots the multiple reflection coefficient amplitude versus concrete material's thickness for the TE and TM polarised 60-degree incident wave under 6 GHz, 28 GHz, 60 GHz. As the material thickness increases, the envelope of the multiple reflection coefficient first fluctuates and then gradually converges to a constant value. The convergence speed varies with the wavelength: the incident wave under higher frequency band converges faster than under lower frequency bands, respectively. Besides, the fluctuation magnitude of the TM polarised incident waves are much severer than the TE polarised waves.

In mmW band, another physical phenomenon cannot be neglected is diffuse scattering from building materials. The propagation channel models of the microwave frequency band and the mmW band are substantially different [47]. Unlike the propagation mechanism at low frequency

bands, mmW propagation channel is more prone to diffraction than to scattering or reflection. This is ascribed to the much smaller wavelength compared with the size of physical objects on the order of cm or m. MmW signals are more sensitive to the tiny lapse in the physical size of objects.

Meanwhile, in the context of communications at low frequency bands, e.g. 6 GHz, the thickness of a wall is comparable to the cm wavelength and surface irregularities on the order of hundreds of m can hardly affect the EM wave's Fabry-Perot resonance phenomenon [48]. However, in mmW communications, the surface irregularities are comparable to the mm wavelength, and the rough surface of a wall would influence the time and angle dispersion of mmW signals caused by diffuse scattering.

Following the widely-used directive model in [49], the general expression of the scattered wave can be modelled as

$$\left|\overline{E_S}\right|^2 = {E_{S0}}^2 \cdot \left(\frac{1+\cos\psi_R}{2}\right)^{\alpha_R} = \left(\frac{SK}{r_i r_S}\right)^2 \frac{dS\cos\theta_i}{F_{\alpha_R}} \cdot \left(\frac{1+\cos\psi_R}{2}\right)^{\alpha_R}, \quad (3\text{-}7)$$

where

$$F_{\alpha_R} = \frac{1}{2^{\alpha_R}} \sum_{j=0}^{\alpha_R} \left[\frac{2\pi}{j+1} \cdot \left\{ \cos\theta_i \cdot \sum_{w=0}^{(j-1)/2} \binom{2w}{w} \cdot \frac{\sin^{2w}\theta_i}{2^{2w}} \right\}^{\left(\frac{1-(-1)^j}{2}\right)} \right]. \quad (3\text{-}8)$$

In the above equation, θ_i is the incident angle, dS is the rough tile length, r_i and r_s denote the distance of the incident part and scattered path of the DS path, S^2 determines the proportion of scattered power from total incident power.

3.1.3. Furniture and equipment setups

There are some things that are common for both offices and conference rooms. However, because the destination of those environments is different, most furniture will be present in different numbers and set up.

In the conference rooms the most important and impactful furniture are tables and chairs. The set ups of the conference rooms depend on the number, shape, and placement of them. Additional equipment present in conference rooms are UEs and personal belongings of the delegates (electronic devices, bottles of water).

In offices commonly present are also computers, computer screens, bookshelves, and cases.

The furniture and equipment setups for conference rooms are mainly classified into the following four types, the typical examples of which are illustrated in Fig. 3-4.

- Table in the middle - chairs are placed around the (round, oval, square, rectangular) table; in front of each chair UE is placed.
    - Areas next to the walls and in the corners don't have to be served.
- School shape - there is a presidium desk in front of the audience. The audience is placed in the (straight or curved) rows. Additionally, next to the presidium desk it may be a lecturer table. The person in front may stand, while the audience is sitting. There is a UE in front of each chair and at the lecturer table.

- Theatre shape - considers only the listening audience.
- Random shape-movable desks
    - Good coverage is necessary, because devices may be placed in any spot of the room.

(a)

(b)

(c)

(d)

Fig. 3-4 Several typical examples of furniture and equipment setup in conference rooms. (a-b) Table in the middle; (c-d) School shape.

Considering the deployment of conference network devices, we should characterise:

- AP location: Indoor APs with large-scale MIMO antenna arrays would commonly be deployed in the vicinity of a wall to avoid any possible negative impact on the functionality and appearance of a conference room.
- UE location: Randomly distributed in the service area.

3.1.4. Challenges

First and foremost, we should notice the standard adopted for audio and video conferencing, e.g., the downlink MU-MIMO transmission can serve up to eight UEs since the maximum number of spatial streams per AP is eight, according to IEEE 802.11ay. Meanwhile, the wireless transmissions for audio and video conferencing should meet the very stringent requirements, i.e., ultra-high reliability and low latency.

The following challenges are brought about by the mmW channel characteristics: first, the channel is time-varying and dynamic, which increases the burden on channel estimation. Second, mmWs are sensitive to blockages. Not only can the surrounding furniture block the signal, but also the conference participants could be regarded as human blockages. Hence, the favourable LOS conditions may not be available when serving users. And the NLOS condition should be paid attentions. Third, mmW propagation experiences complicated EM phenomena, e.g., the diffuse scattering is non-negligible in mmW bands but can be ignored in microwave bands. Fourth, mmW communications are usually confined in a short range, which is not friendly to long-distance transmissions in a large conference room.

3.2. Modelling for video conferencing

Video conferencing is when next to the main audio system the camera system is working. With camera system additional features like broadcasting or recording might be apply as well. Video conference allows participants who are far away from each other to have face-to-face meeting. It also applies to meetings in the same room with large number of participants, or to hybrid meetings. In the two latest cases the video is often displayed on the large screen in the room.

The requirements for camera system are as follows:

- The active speaker should be shown. When there is possibility to have more than one active speaker during a discussion the number of participants' video should be choose.
- The overview of the room should be displayed when there is no active speaker.
- The moving camera image should be avoided.
- Camera system never can be the leading system in the conference. It should be a support for the main medium.

Suitable resolution and codecs should be chosen for the size of screen and the network's capacity and transmission standard.

3.2.1. Latency and video quality requirements

Video should be a support for the sound in the video conferencing. That means, the synchronization is necessary. When video has too much delay or appears much faster than sound it is a large inconvenience. In completely remote video conferencing that one requirement is enough, but for the video conference hold in one room additional requirement for audio latency is made. It is because person displayed on the screen is also visible in person, and there can't be too much delay between speaker's voice and the sound in the audio system.

According to the ITU-R BT.1359-1 standard video should be displayed maximum 30 ms before audio or 22.5 ms after it. For audio the maximum latency is 20 ms.

During video conference the image shows the speaker on the (mostly) unchanged background. Thus, quality requirements are similar for those in the news broadcasting.

3.3. Performance evaluation under different MIMO configurations

3.3.1. SU-MIMO

In this subsection, we discuss the case that only one user per subframe is scheduled in the whole band. We consider indoor LOS MIMO downlink transmissions in the cubic room defined in 3.1, as shown in Fig. 3-5. In the considered room, one BS is deployed close to one of the walls and one UE could be arbitrarily positioned. The BS is deployed in parallel with one of the walls with a small distance of from the wall.

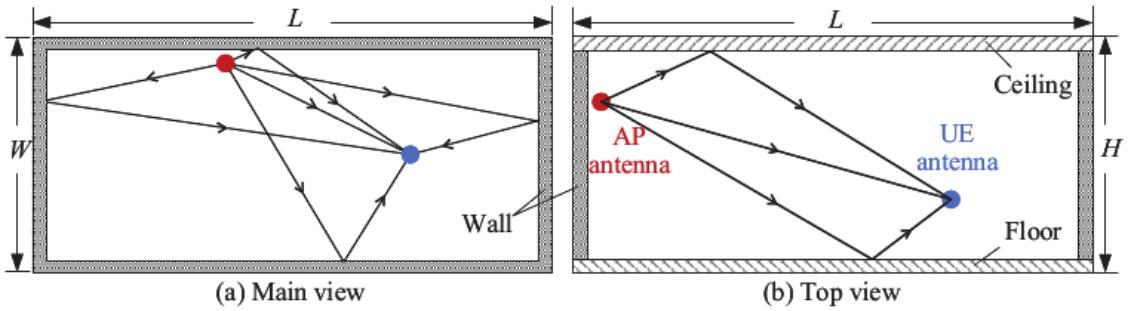

Fig. 3-5. The reflection model in a conference room

The BS and a typical UE are equipped with N_T and N_R omnidirectional antennas, respectively, both in linear arrays with inter-antenna spacing D. The complex frequency-flat linear channel from the BS to the typical UE is constructed as

$$\mathbf{y} = \mathbf{H}\mathbf{x} + \mathbf{n}, \tag{3-9}$$

where $\mathbf{x} \in \mathbb{C}^{N_T \times 1}$, $\mathbf{y} \in \mathbb{C}^{N_R \times 1}$ denote the transmitted signal and the received signal, respectively, denotes the additive white Gaussian noise, and $\mathbf{H}$ is a $N_R \times N_T$ channel matrix.

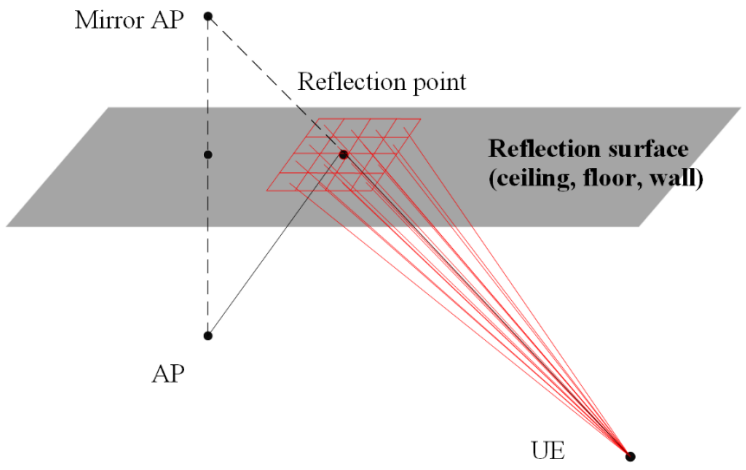

Fig. 3-6. The diffuse scattering model in a conference room

For a certain position in the room and based on planar wave assumption, the LOS path, the WR path, and the DS path from one of the wall are deterministically modelled by Friis' formula as $N_R \times N_T$ matrix $\mathbf{H}_{LOS}$, $\mathbf{H}_{WR}$ and $\mathbf{H}_{DS}$, respectively, whose elements are given as

$$[\mathbf{H}_{LOS}]_{n_R, n_T} = \frac{\mu}{4\pi d_1} e^{-j\frac{2\pi}{\mu}\left(d_1 + D\left(\left(n_R - \frac{N_R-1}{2}\right)\cos\theta_{R_1} + \left(n_T - \frac{N_T-1}{2}\right)\cos\theta_{T_1}\right)\right)}, \tag{3-10}$$

$$[\mathbf{H}_{\mathrm{WR}}]_{n_{\mathrm{R}},n_{\mathrm{T}}} = \frac{\mu\Gamma}{4\pi d_2} e^{-j\frac{2\pi}{\mu}\left(d_2 + D\left(\left(n_{\mathrm{R}} - \frac{N_{\mathrm{R}}-1}{2}\right)\cos\theta_{\mathrm{R}_2} + \left(n_{\mathrm{T}} - \frac{N_{\mathrm{T}}-1}{2}\right)\cos\theta_{\mathrm{T}_2}\right)\right)}, \quad (3\text{-}11)$$

$$[\mathbf{H}_{\mathrm{DS}}]_{n_{\mathrm{R}},n_{\mathrm{T}},t_a,t_b} = \frac{\mu\chi}{4\pi\sqrt{d_{3,t_a,t_b} d_{4,t_a,t_b}}} e^{-j\frac{2\pi}{\mu}\left(d_{3,t_a,t_b} + d_{4,t_a,t_b} + D\left(\left(n_{\mathrm{R}} - \frac{N_{\mathrm{R}}-1}{2}\right)\cos\theta_{\mathrm{R}3,t_a,t_b} + \left(n_{\mathrm{T}} - \frac{N_{\mathrm{T}}-1}{2}\right)\cos\theta_{\mathrm{T}3,t_a,t_b}\right)\right)}, \quad (3\text{-}12)$$

in which $n_{\mathrm{T}} \in \{0, 1, \ldots, N_{\mathrm{T}} - 1\}$ and $n_{\mathrm{R}} \in \{0, 1, \ldots, N_{\mathrm{R}} - 1\}$ are the indices of transmit and receive antenna elements, μ denotes the wavelength of EM waves in the air, d_1 and d_2 denote the length of the LOS path and the WR path, respectively, θ_{T_1} and θ_{T_2} denote the approximated angle of departure (AoD) of the LOS path and the WR path at the BS array, respectively, while θ_{R_1} and θ_{R_2} denote the approximated angle of arrival (AoA) of the LOS path and the WR path at the UE array, respectively, and Γ represents the equivalent reflection coefficient of the WR path. Along the WR path, multiple internal reflections are considered when the EM wave interacts with the building material. Considering the building material as a single-layer dielectric reflector, in (3-12), t_a and t_b denote the index of a rough scattering tile with the length dS around the reflection point, as shown in Fig. 3-6, respectively, d_{3,t_a,t_b} and d_{4,t_a,t_b} denote the distance between the (t_a, t_b) scattering tile and the AP and between the (t_a, t_b) scattering tile and the UE antenna, respectively, $\theta_{\mathrm{T}3,t_a,t_b}$ and $\theta_{\mathrm{R}3,t_a,t_b}$ denote the AOD and AOA of the DS path through the (t_a, t_b) scattering tile, respectively, and χ is the DS coefficient.

Then the channel model for the UE is given by

$$\mathbf{H} = \mathbf{H}_{\mathrm{LOS}} + \mathbf{H}_{\mathrm{WR}} + \mathbf{H}_{\mathrm{DS}}, \quad (3\text{-}13)$$

And the corresponding channel capacity is given by

$$C = \log_2\left(\left|I_{N_{\mathrm{R}}} + \frac{\rho}{N_{\mathrm{T}}}\mathbf{H}\mathbf{H}^{\mathrm{H}}\right|\right). \quad (3\text{-}14)$$

3.3.2. MU-MIMO

In this subsection, we discuss the case that each AP can schedule $K \leq 8$ users simultaneously per resource block. Under spherical wave assumption, the element of the *K*-by-*M* channel matrix $\mathbf{H}$ is deterministically modelled by

$$h_{k,m} \propto \frac{1}{D_{k,m}}\exp\left(-j\beta D_{k,m}\right) + \sum_{i=1}^{6}\frac{\Gamma_{k,m,i}}{d_{k,m,i}}\exp\left(-j\beta d_{k,m,i}\right) + \sum_{i=1}^{6}\sum_{t_a=1}^{T_a}\sum_{t_b=1}^{T_b}\frac{\chi_{k,m,i,t_a,t_b}}{d_{k,m,i,t_a,t_b}}\exp\left(-j\beta d_{k,m,i,t_a,t_b}\right), \quad (3\text{-}15)$$

Zero-forcing precoding is adopted to eliminate inter-stream interference. The precoding matrix $\mathbf{W} \in \mathbb{C}^{M\times K}$ is given as

$$\mathbf{W} = [\mathbf{w}_1\mathbf{w}_2\ldots\mathbf{w}_K] = \mathbf{H}^{\mathrm{H}}\left(\mathbf{H}\mathbf{H}^{\mathrm{H}}\right)^{-1}, \quad (3\text{-}16)$$

Hence the received signal at UE is described as

$$y_k = \mathbf{h}_k\mathbf{w}_k s_k + \mathbf{h}_k\sum_{i=1, i\neq k}^{K}\mathbf{w}_i s_i + n_k, \quad (3\text{-}17)$$

where s_i is the data symbol intended to UE i, and n_k is the additive white Gaussian noise received at UE k.

The sum rate of K users is given by

$$R = \sum_{k=1}^{K} \log_2 \left(1 + \frac{\mathbf{h}_k \mathbf{w}_k P \mathbf{h}_k^{\dagger} \mathbf{w}_k^{\dagger}}{\sum_{i=1, i \neq k}^{K} \mathbf{h}_i \mathbf{w}_i P \mathbf{h}_i^{\dagger} \mathbf{w}_i^{\dagger} + \sigma_n^2} \right), \quad (3\text{-}18)$$

3.3.2.1. MU grouping techniques

In MU grouping there are three aspects that should be taken into account. They are the number of groups, the number of STAs within the group, and the requirements to put the STAs into the same (or separate) groups. In [50] the authors considered the OFDMA technique and presented the grouping method which can separate users into different groups. They also proposed an adaptive algorithm to adjust the group number and improve the system performance.

Considering the fixed number of STAs, limited bandwidth, and equal division we can assume that when the number of groups is small, the number of STAs in each of them is large. On the contrary, when the number of groups is large, the number of STAs in each of them is small. In the first case, the spectrum allocated to each group increases, but SINR decreases, thus performance may become poor. In the second case, the SINR increases, but the allocated bandwidth decreases. The performance is also hard to improve.

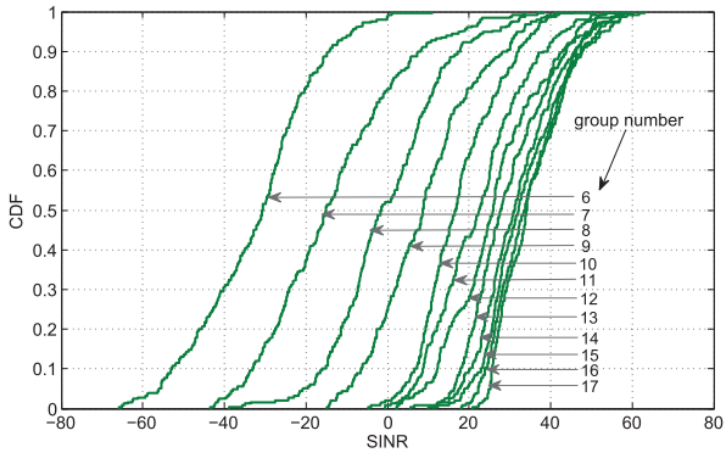

Fig. 3-7. SINR with different group numbers (M = 64, K = 50, (D, φ) = (50, 5°)) [50]

For different numbers of STAs (user number) three different algorithms were compared in Fig. 3-7. The best sum-rate was obtained for each simulation when the algorithm with an adaptive number of multi-user groups was proposed. It shows that the number of groups and the number of STAs in them should depend on the total number of STAs to serve.

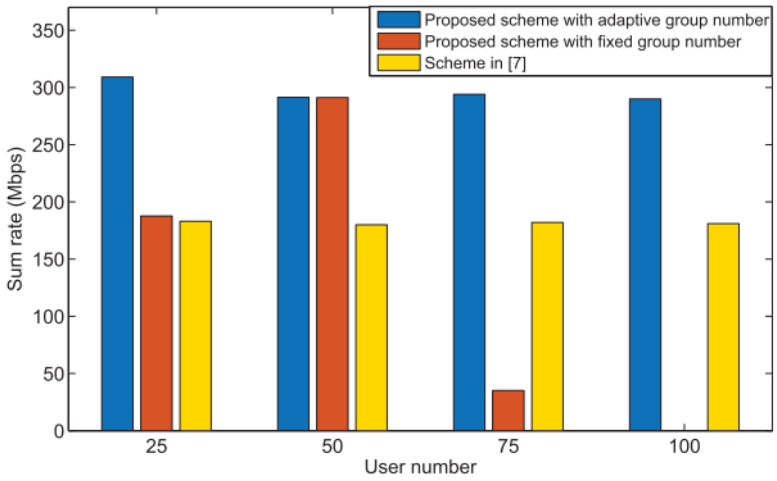

Fig. 3-8. Sum rates obtained in different schemes (M = 64, K = (25, 50, 75, 100), (D, φ) = (50, 5°)) [50]

Regarding the rule applied to separate or group two different STAs together, the correlation among them is considered. Authors in [50-53] agree that the channel correlation between STAs can significantly affect the system performance in MU-MIMO systems. They advise putting highly correlated STAs to different groups. It is because more power is needed to eliminate the interference between STAs when the spatial correlation is large.

3.3.2.2. Centralized MIMO techniques

In this subsection, we study the centralized MIMO configurations in a $32\times 12\times 4\ m^3$ rectangular conference room. The AP is equipped at the height of 2.5 m with the distance of 0.05 m to one of the walls with the thickness of 0.2 m. The considered room consists of 4 concrete walls, one floor, and one ceiling. Note that for indoor conference scenarios, the users served at a time are usually grouped according to their spatial distribution because the same audio/video content should be transmitted to all users in a scheduled manner. We assume to serve 8 users at a time using 60 GHz bands, who are sitting at the same height of 0.8 m and uniformly distributed in one of the four possible user areas. We consider both LOS and NLOS conditions.

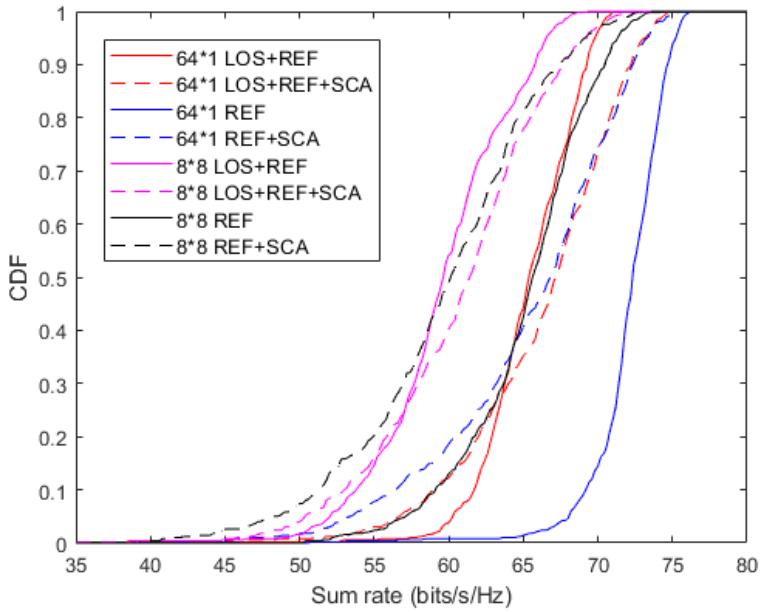

Fig. 3-9. The CDF of sum rates under LOS and NLOS conditions using 64 antennas for a centralized MIMO configuration

From Fig. 3-9, we observe that the NLOS cases (i.e., the blue and black dashed or solid curves) have a wider range in the sum rate than the LOS cases. Besides, the signals along the DS path contribute significantly to the sum rate in both LOS cases and NLOS cases, as up to 10 bits/s/Hz difference in capacity when considering with or without scattering, meaning that the DS phenomenon cannot be ignored in the bands of 60 GHz. Meanwhile, it is found that, both in LOS and NLOS cases, the configuration of 64x1 or 8x8 of the MIMO antenna array has little impact on the sum rate.

3.3.2.3. Antenna selection techniques

In this subsection, we propose two subarray selection schemes to exploit the spatial diversity.

Group selection (GS): Half number of the subarrays are selected according to the user distribution. In order to reduce the spatial correlation among selected antennas and reduce selection overhead, the subarrays near the same wall are grouped. In each group, half of the subarrays that have relatively good channel condition will be selected to serve the given 8 users. For example, if there are totally 8 subarrays, with 2 subarrays near each wall. We will select 4 subarrays in total from 4 walls, each one providing better channel condition compared with the other one subarray.

Random selection (RS): Half number of the subarrays are randomly selected, as a comparison.

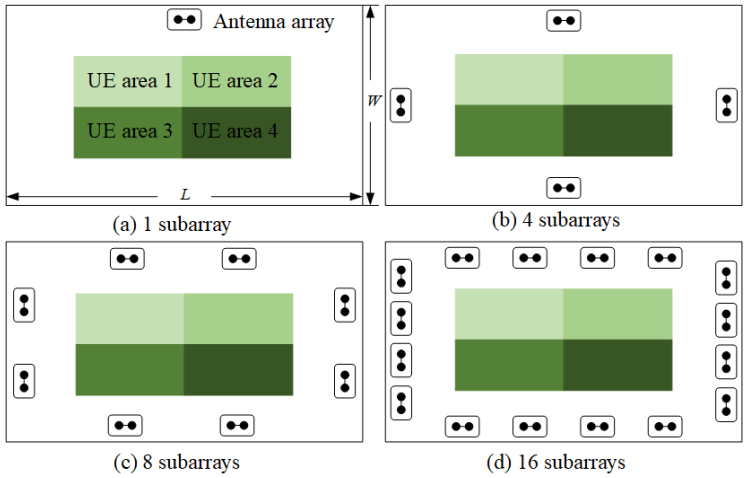

Fig. 3-10. Four distributed MIMO subarray configurations in a rectangular conference room

We only consider LOS conditions in the comparison of the distributed MIMO subarray configurations using GS and RS. The simulation assumptions in Figs. 3-11, 3-12,3-13 are the same as that of Fig. 3-9.

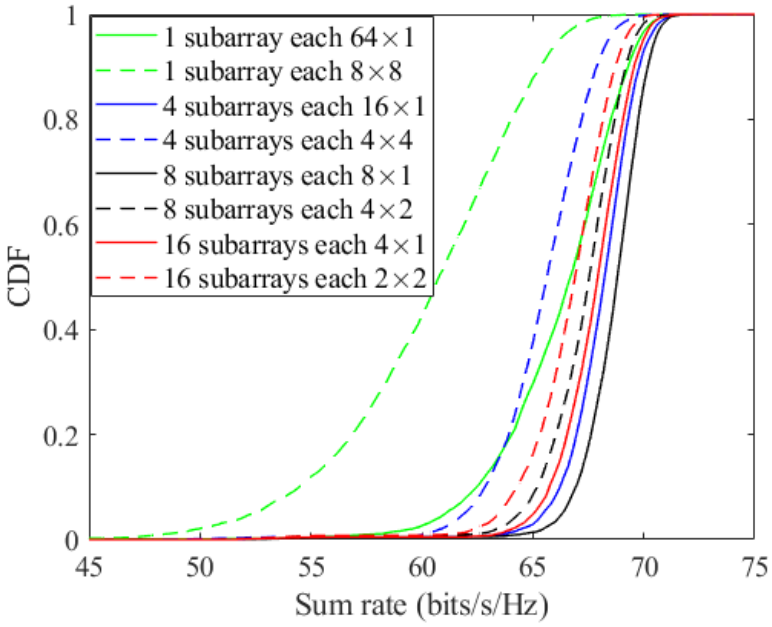

Fig. 3-11. The CDF of sum rates using 64 antennas under 1,4, 8, 16 subarray configurations

As shown in Fig. 3-11, as the number of subarrays increases from 1 to 8, the sum rate increases. That is because the spatial diversity is exploited. Moreover, the 8-subarray case has very similar performance as the 16-subarrays. Hence, 8 subarrays in total is enough for the given room.

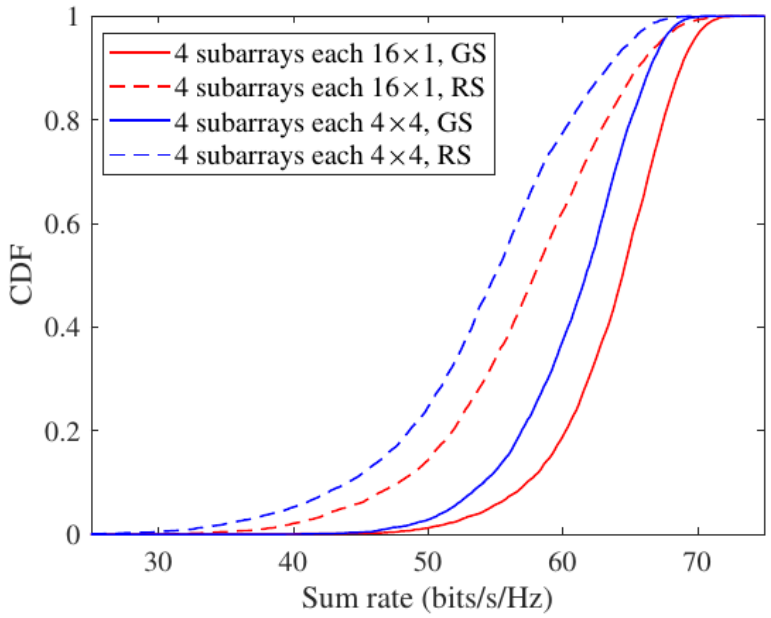

Fig. 3-12. The CDF of sum rates using 64 antennas under 4 subarray configurations

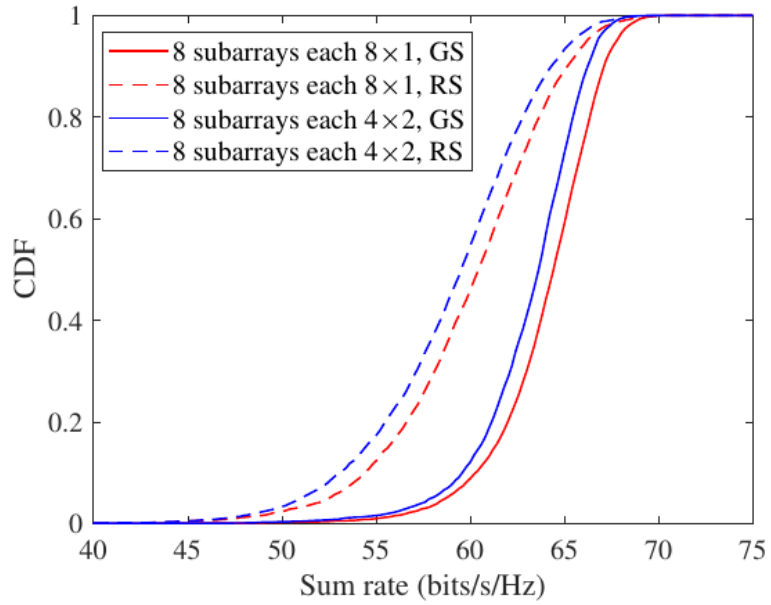

Fig. 3-13. The CDF of sum rates using 64 antennas under 8 subarray configurations

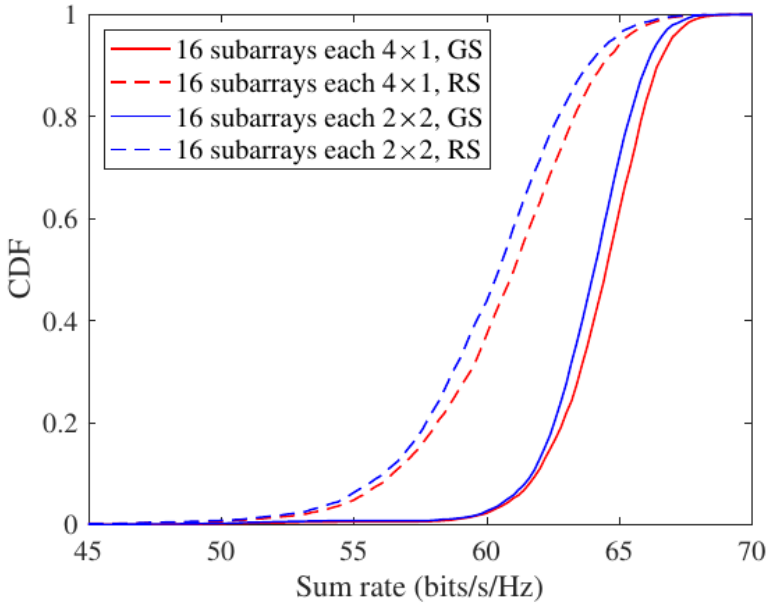

Fig. 3-14. The CDF of sum rates using 64 antennas under 16 subarray configurations

The results in Figs. 3-11,3-12,3-13 are based on 64 transmit antennas in total, where half number of the subarrays (32 antennas) are selected according to the user selection. In the 4-subarray case, we select the 2 subarrays with the best channel condition. Hence, the diversity is just from two walls, not four. We can see from the figures that GS is always superior to RS. Again, the 16-subarray case has very similar performance with the 8-subarray case.

4. Developing signal processing solutions for mmW massive MIMO

4.1. Cell-free mmW massive MIMO systems

A solution to enhance connectivity whenever and wherever, is cell-free massive MIMO. Cell-free massive MIMO has been defined as an implementation of the massive MIMO but, in this case, there is a considerably higher amount of APs than UEs, being these APs distributed over a wide area, and connected to a single central processing unit (CPU) via front-haul, which controls network synchronization, power allocation and data streams. Each AP and UE can have one or more antennas [54].

In a similar way to conventional massive MIMO, time division duplexing (TDD) is the preferred duplexing method, since the overhead generated by it does not depend on the number of APs, depending only on the number of users, which means that more APs will not decrease performance due to more overhead, so performance will increase with the number of APs [54]. As stated in [55], cell-free massive MIMO leads to “uniformly great service for everyone". This is due to the fact that, spreading a large number of APs over an area implies that users will have several APs close to them, which redounds in lesser path losses, as well as more macro-diversity, resulting all this in higher and more evenly distributed per-user throughput. Another advantage offered by cell-free massive MIMO is its power efficiency, which can be achieved thanks to the distributed architecture, that makes possible to deliver power only to a subset of APs for each user without decreases in performance, which in turn increases power efficiency [54]. Favorable propagation occurs when there is a high number of APs, resulting in channel vectors established between the AP and each UE being orthogonal (or almost) and, owing to this phenomenon, higher spectral efficiency (SE) can be achieved due to the lower inter-user interference. Moreover, as stated in [54], “cell-free massive MIMO can achieve very good performance with simple linear processing such as maximum-ratio or zero-forcing processing”.

4.2. Digital precoding

How to achieve the optimum beamforming design is challenging. Analog beamforming is the simplest to implement, but the phase shifters can only be adjusted to form one angular beam, what limits to one the number of users that can be served at a time. On the other hand, hybrid BF has a middle implementation complexity between the analog and digital approaches. However, the hybrid approach, despite of being able to create multiple angular beams, can only transmit one phase per signal and the same power on all antenna elements. This latter issue reduces the possibility of using power allocation strategies. Digital beamforming, otherwise, offers full flexibility, given the chance of transmitting any signal via any antenna element.

In this work, digital beamforming concept in massive MIMO mmW systems, will be referred as precoding, since in massive MIMO precoding concept is used to define a fully digital implementation [56].

It is worth to mention that research community in the past years has shown certain reluctance to fully digital techniques, due to the complexity of hardware implementation. Notice that for massive MIMO antenna arrays, the design of fully digital transceivers implies as many RF chains as antenna elements, which in most of the cases involves high power consumption. Nevertheless, low-power consumption fully digital approaches are arising [57], which encourage to research in depth on optimal precoding techniques for mmW massive MIMO systems.

Precoding techniques should meet two main requirements: to avoid interference and to adapt continuously to the sudden channel changes in high-mobility scenarios.

In the case of fully digital approaches, data processing is only applied to the base band signal, significantly reducing the complexity in the design of the base band weighting matrix. In this sense, with the maximum radio transmission (MRT) technique the base band weighting matrix is optimized to maximize the received signal at the user's site, while the zero forcing technique can be applied to minimize interference.

4.3. Precoding optimization

The optimization of the power control coefficients has been studied in [58,59]. The constraints under which the problem is analyzed vary depending on the use case and the interest of each author.

In [58], the authors studied power optimization algorithms for both cell-free massive MIMO systems and SC systems. Sub-optimal power allocation solutions are proposed based on conjugate beamforming and zero-forcing precoders. The results show that higher rates are achievable when implementing cell-free massive MIMO systems instead of SC systems. In [59] the power coefficients are also optimized but this time looking forward to satisfying per-user quality of service (QoS) and per-AP transmit power constraints when maximizing the energy efficiency in downlink. In this work, the authors also considered the case where the channel state information (CSI) is not perfectly known

In order to improve the overall energy efficiency of the system, not only power saving solutions for the downlink have been studied, but also solutions for the uplink. In this sense, some mechanisms for controlling the power emitted from the user side have been proposed in [49, 50]. More precisely, in [50] the authors focused on the optimization in the selection of pilot powers with the objective of mitigating the pilot contamination. In consequence, higher throughputs are achieved when implementing the proposed solution. Moreover, in [61] a max-min SINR problem is solved by optimizing the power coefficients in uplink. The solution proved to outperform considerably the existent algorithms in terms of rate per user.

So far, the aforementioned works were carried out for under 6 GHz frequency band. However, the energy efficiency maximization for cell-free massive MIMO systems at mmW has been also investigated in [53]. In [53], the authors addressed the problem considering hybrid precoding architectures. The results obtained demonstrated the increase of energy efficiency with respect to uniform power allocation schemes but also a considerable performance degradation when comparing with fully digital precoding solutions.

In this work, fully digital precoding is considered. Then, for a max-min fairness (MMF) optimization problem is solved aiming at maximizing the minimum spectral efficiency of a specific user.

4.4. Overcoming human body blockage effects

4.4.1. Distributed deployment solutions

For the sake of study, we chose the industrial indoor scenario described in [62,63]. The scenario was modelled as an open area of 100 m x 100 m to resemble an industrial warehouse. In the

scenario there are no blocking objects or structures, except the human bodies. The channel was implemented following [64], specifically, the model InH_B. For the use case, 400 directive antennas were considered for 4 different configurations, which is shown in Fig. 4-1:

- C-1: 4 APs equipped with 10 x 10 antenna array each and power transmission per AP equal to 21 dBm.
- C-2: 16 APs equipped with 5 x 5 antenna array each and power transmission per AP equal to 15 dBm
- C-3: 25 APs equipped with 4 x 4 antenna array each and power transmission per AP equal to 13 dBm.
- C-4: 100 APs equipped with 2x2 antenna array each and power transmission per AP equal to 7 dBm.

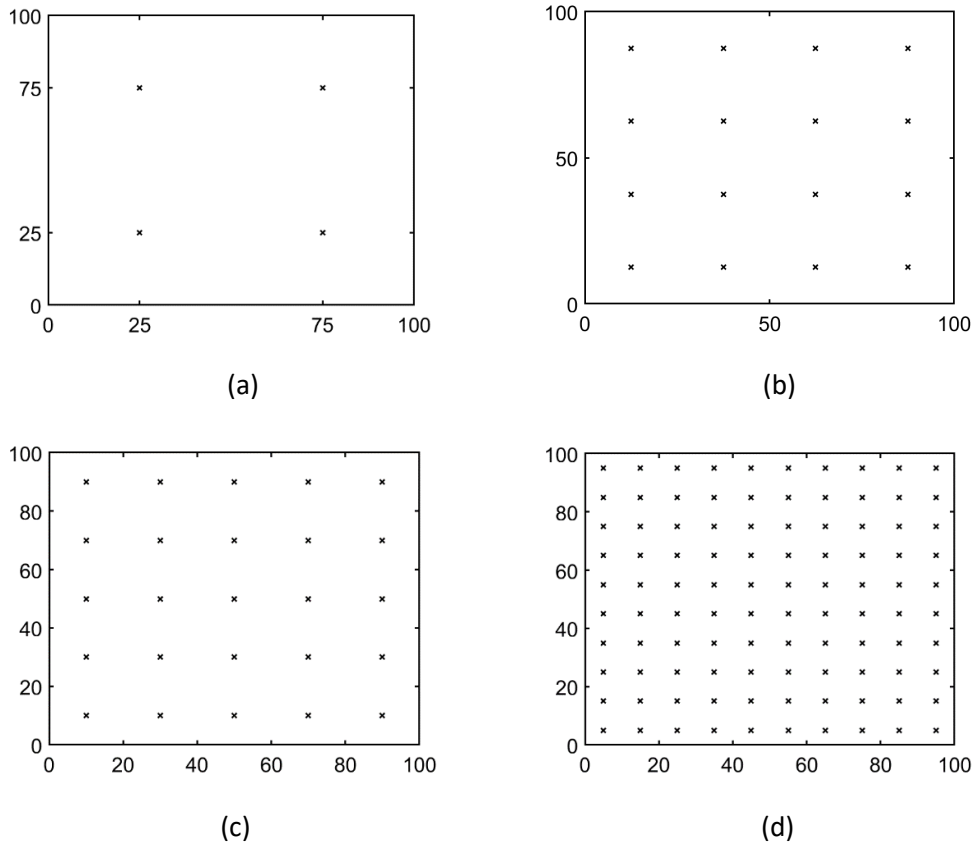

Fig. 4-1. APs deployments for industrial scenarios described as a) C-1, b) C-2, c) C-3, d) C-4.

The parameters of each individual antenna element are as in [65]. In all cases the APs were uniformly distributed as it can be seen in Fig. 4-1 and attached to the ceiling at 6 m of height. The frequency was set up at 30 GHz and bandwidth equal to 80 MHz. The simulations have been carried out for different number of uniformly distributed users: 20, 50, 100 and 200 users. The height of the users and the UE are 1.7 m and 1.5 m, respectively. The rest of parameters, that have not been mentioned, were taken from [63].

4.4.2. Design of precoders

It is worth to mention that in this study, fully digital hardware is considered. That gives us the highest grade of freedom to play with the power and phases through the precoding algorithms.

With digital precoding, it is possible to transmit any signal, with any phase and any power through any antenna. Specifically, we have chosen MMF power allocation scheme [63]. This algorithm seeks to maximize the minimum spectral efficiency by selecting the accurate power coefficients for each antenna element. As the result, the maximum spectral efficiency value per user will not be achieved, but all users will be benefited in a similar way. In cell-free mmW massive MIMO systems with user-centric approaches, it is possible for the users to select the best APs based on the received power or the channel quality [63], however this is out of the scope of this work. In our use case, all APs transmit to all users at the same time.

4.5. Results

The simulations have been carried out for the four aforementioned configurations without considering body blockage and considering body blockage. The Fig. 4-2 shows the cumulative distribution function of the spectral efficiency for each user for all cases. First of all, and to make a clearer analysis we should interpret the graph in two steps: impact of the density of the deployment and impact of the body blockage.

If we focus on any curve pattern (solid or dotted), it can be seen that the SE improves with the APs's increase independently of the body blockage consideration. However, the increase is limited, since as the curves in red, blue, and green show, the performance is very similar among them. This suggest the existence of a limit for densification even when coherent transmission is considered and in consequence, the interference strongly mitigated. On the other hand, the shape of the curves indicates fairer resource allocation for denser deployments. It is worth to remind at this point that for all configurations the number of antennas and total power transmission are kept. Then, the performance changes experienced in each configuration are completely due to the configuration itself.

In another vein, if we group the curves by pattern, roughly speaking, it can be seen that the curves that consider blocking are worse than the case where blocking is not considered.

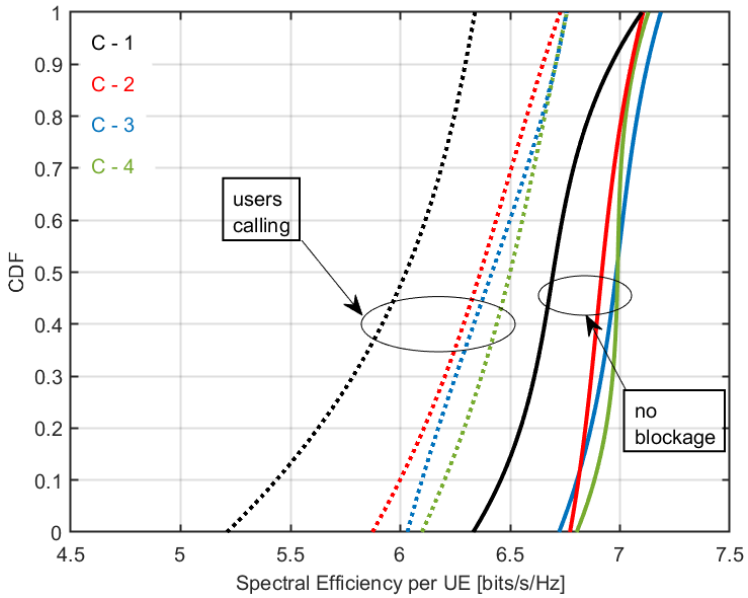

Fig. 4-2. Spectral Efficiency for all configurations applying MMF precoding optimization.

5. Conclusions

In this report, we have presented our work to jointly optimize massive MIMO configurations and RF properties of BEs for mmW SC deployment.

In Chapter 2, we have provided a general analytical framework for a 3D mmW SC network utilizing stochastic geometry. Directional beamforming with a sectored BS antenna model and a 3D blockage model have been considered in the analysis. The BSs, UEs and blockages are assumed to be distributed according to independent PPPs, where their heights are modeled as well. Under these assumptions, we have derived the expressions of LOS probability and ASE. The analytical and numerical results show that when the BS heights are higher than the UE heights, the ASE will first increase and then decrease with the BS density and that there exists a BS density that maximizes the ASE.

In Chapter 3, in order to optimize the mmW massive MIMO configurations for indoor offices and large conference rooms, we have modelled the BE setups and wireless channel considering both reflection and diffuse scattering propagation phenomena. The key BE setup parameters include the room's dimensions, furniture setup, the destiny of the room, and building material properties. The key wireless system requirement parameters include the exact frequency bandwidth to define the path loss and the influence of the obstacles and propagation phenomena, the type of data in the network to know the required throughput, the number of UEs, and the type of MIMO technique to schedule the transmission. Then, we have provided the performance evaluation for SU-MIMO and MU-MIMO configurations in terms of their capacity. Our results reveal that the highly correlated UEs should be put into different user groups, and that the appropriate design of distributed MIMO configuration with the subarray-based antenna selection can increase the sum rate of the MU-MIMO system.

In Chapter 4, we have analyzed the effects of body blockage on the performance of cell-free mmW massive MIMO systems in indoor environments. Specifically, we have evaluated the impact of body blockage on spectral efficiency while considering different AP configurations. It has been spotted that the effects of body blockage are more detrimental for less well-spread AP and antenna distributions. For deployments with higher AP density, higher values of SE and greater fairness among users are obtained. Nevertheless, the increase of SE is limited, which indicates that there is no point in increasing the number of APs beyond this point of saturation.

References

[1] K. Venugopal, M. C. Valenti and R. W. Heath, “Device-to-device millimeter wave communications: interference, coverage, rate, and finite topologies,” IEEE Trans. Wireless Commun., vol. 15, no. 9, pp. 6175-6188, Sept. 2016.

[2] T. Bai, R. Vaze and R. W. Heath, “Analysis of blockage effects on urban cellular networks,” IEEE Trans. Wireless Commun., vol. 13, no. 9, pp. 5070-5083, Sept. 2014.

[3] M. Kamel, W. Hamouda and A. Youssef, “Ultra-dense networks: a survey,” IEEE Commun. Surveys Tut., vol. 18, no. 4, pp. 2522-2545, Fourth quarter, 2016.

[4] J. G. Andrews, F. Baccelli, and R. K. Ganti, “A tractable approach to coverage and rate in cellular networks,” IEEE Trans. Commun., vol. 59, no. 11, pp. 3122-3134, Nov. 2011.

[5] J. G. Andrews, X. Zhang, G. D. Durgin and A. K. Gupta, “Are we approaching the fundamental limits of wireless network densification?” IEEE Commun. Mag., vol. 54, no. 10, pp. 184-190, Oct. 2016

[6] J. Liu, M. Sheng, L. Liu and J. Li, “Network densification in 5G: from the short-range communications perspective,” IEEE Commun. Mag., vol. 55, no. 12, pp. 96-102, Dec. 2017.

[7] J. Liu, M. Sheng, L. Liu, and J. Li, “Effect of densification on cellular network performance with bounded pathloss model,” IEEE Commun. Lett., vol. 21, no. 2, pp. 346-349, Feb. 2017.

[8] M. Ding, P. Wang, D. L´opez-P´erez, G. Mao, and Z. Lin, “Performance impact of LoS and NLoS transmissions in dense cellular networks,” IEEE Trans. Wireless Commun., vol. 15, no. 3, pp. 2365-2380, Mar. 2016.

[9] M. Ding and D. L´opez-P´erez, “Performance impact of base station antenna heights in dense cellular networks,” IEEE Trans. Wireless Commun., vol. 16, no. 12, pp. 8147-8161, Dec. 2017.

[10] E. Bjornson, et al., “Massive MIMO in sub-6 GHz and mmWave: physical, practical, and use-case differences,” IEEE Wireless Communications, vol. 26, no. 2, pp. 100-108, April 2019.

[11] E. Torkildson, et al., “Indoor millimeter wave MIMO: feasibility and performance,” IEEE Trans. Wireless Commun., vol. 10, no. 12, pp. 4150- 4160, Dec 2011.

[12] V. Raghavan, et al., “Millimeter-wave MIMO prototype: measurements and experimental results,” IEEE Commun. Mag., vol. 56, no. 1, pp. 202-209, Jan. 2018.

[13] E. Bj¨ornson, L. Sanguinetti, H. Wymeersch, J. Hoydis, and T. L. Marzetta,“ Massive mimo is a reality—what is next?: Five promising research directions for antenna arrays,” Digital Signal Processing, vol. 94, pp.3–20, 2019.

[14] H. Q. Ngo, A. Ashikhmin, H. Yang, E. G. Larsson, and T. L. Marzetta, “Cell-free massive MIMO versus small cells,”IEEE Transactions onWireless Communications, vol. 16, no. 3, pp. 1834–1850, mar 2017.

[15] J. Kibiłda, A. B. MacKenzie, M. J. Abdel-Rahman, S. K. Yoo, L. G.Giordano, S. L. Cotton, N. Marchetti, W. Saad, W. G. Scanlon, A. Garcia-Rodriguez, D. López-Pérez, H. Claussen, and L. A. DaSilva, “Indoor millimeter-wave systems: Design and performance evaluation,” Proceedings of the IEEE, vol. 108, no. 6, pp. 923–944, 2020.

[16] M. Alonzo, S. Buzzi, A. Zappone, and C. D’Elia, “Energy-efficient power control in cell-free and user-centric massive MIMO at millimeter wave,” IEEE Transactions on Green Communications and Networking, vol. 3,no. 3, pp. 651–663, Sep 2019.

[17] V. Petrov, M. Komarov, D. Moltchanov, J. M. Jornet and Y. Koucheryavy, “Interference and SINR in millimeter wave and terahertz communication systems with blocking and directional antennas,” IEEE Trans. Wireless Commun., vol. 16, no. 3, pp. 1791-1808, Mar. 2017.

[18] A. K. Gupta, J. G. Andrews and R. W. Heath, “Macrodiversity in cellular networks with random blockages,” IEEE Trans. Wireless Commun., vol.17, no. 2, pp. 996-1010, Feb. 2018.

[19] M. M. Azari, F. Rosas, A. Chiumento, and S. Pollin, “Coexistence of terrestrial and aerial users in cellular networks,” in Proc. of IEEE Globecom Workshops (GC Wkshps), Singapore, Dec 2017, pp. 1–6.

[20] J. Yang, M. Ding, G. Mao, Z. Lin, D. Zhang and T. H. Luan, “Optimal base station antenna downtilt in downlink cellular networks,” IEEE Trans. Wireless Commun., vol. 18, no. 3, pp. 1779-1791, Mar. 2019.

[21] V. Petrov, M. Komarov, D. Moltchanov, J. M. Jornet and Y. Koucheryavy, “Interference and SINR in millimeter wave and terahertz communication systems with blocking and directional antennas,” IEEE Trans. Wireless Commun., vol. 16, no. 3, pp. 1791-1808, Mar. 2017.

[22] J. Liu, M. Sheng and J. Li, “Improving network capacity scaling law in ultra-dense small cell networks,” IEEE Trans. Wireless Commun., vol.17, no. 9, pp. 6218-6230, Sept. 2018.

[23] M. U. Sheikh, K. Ruttik, R. Jäntti, and J. Hämäläinen, “Measurements and Ray Tracing Simulations : Impact of Different Antenna Positions on Meeting Room Coverage at 60 GHz,” pp. 63–67, 2020.

[24] A. Maltsev, R. Maslennikov, A. Sevastyanov, A. Khoryaev, and A. Lomayev, “Experimental investigations of 60 GHz WLAN systems in office environment,” IEEE Journal on Selected Areas in Communications, 27(8), 1488-1499, 2009.

[25] A. Al-jzari, J. Towers, and S. Salous, “Characterization of Indoor Environment in the 60 GHz band,” in URSI General Assembly and Scientific Symposium (GASS), 2020.

[26] H. Xu, V. Kukshya, and T. S. Rappaport, “Spatial and temporal characteristics of 60-GHZ indoor channels,” IEEE J. Sel. Areas Commun., 2002.

[27] T. Manabe, Y. Miura, and T. Ihara, “Effects of antenna directivity and polarization on indoor multipath propagation characteristics at 60 GHz,” IEEE J. Sel. Areas Commun., vol. 14, no. 3, pp. 441–447, 1996.

[28] A. C. Austin, D. Guven, M. J. Neve, and K. W. Sowerby, “60 GHz Millimetre-Wave Channel Characterisation for Indoor Office Environments”, In 2019 13th European Conference on Antennas and Propagation (EuCAP) (pp. 1-5). IEEE, 2019

[29] X. Wu, C. X. Wang, J. Sun, J. Huang, R. Feng, Y. Yang, and X. Ge, “60-GHz millimeter-wave channel measurements and modeling for indoor office environments,” IEEE Transactions on Antennas and Propagation, 65(4), 1912-1924, 2017.

[30] M. U. Sheikh, M. El Hajj, R. Jäntti, J. Hämäläinen, G. Zaharia, and G. El Zein, “Channel Characterization and Validation of Ray Tracing Simulations with Measurements at 60 GHz in Office Environment,” 2020.

[31] J. Park, Y. Kim, Y. Hur, K. Lim, and K. Kirn, “Analysis of 60 GHz band indoor wireless channels with channel configurations,” Simulation, pp. 617–620, 1998.

[32] C. Jansen, et al., ``The impact of reflections from stratified building materials on the wave propagation in future indoor terahertz communication systems,'' IEEE Trans. Antennas Propag., vol. 56, no. 5, pp. 1413-1419, May 2008.

[33] A. Asp, et al., ``Radio signal propagation and attenuation measurements for modern residential buildings,'' IEEE Globecom Workshops, Anaheim, CA, 2012, pp. 580-584.

[34] A. Asp, et al., ``Impact of different concrete types on radio propagation: fundamentals and practical RF measurements,'' 4th International Conference on Smart and Sustainable Technologies (SpliTech), Split, Croatia, 2019, pp. 1-8.

[35] A. Asp, et al., ``Impact of modern construction materials on radio signal propagation: practical measurements and network planning aspects,'' IEEE 79th Vehicular Technology Conference (VTC Spring), Seoul, 2014, pp. 1-7.

[36] A. Asp, et al., ``Effect of plastering mesh on radio signals: modelling and practical measurements,'' European Conference on Networks and Communications (EuCNC), Dubrovnik, Croatia, 2020, pp. 68-73.

[37] K. Sato, et al., ``Measurements of reflection and transmission characteristics of interior structures of office building in the 60-GHz band,'' IEEE Trans. Antennas Propag., vol. 45, no. 12, pp. 1783-1792, Dec. 1997.

[38] A. Karttunen, et al., ``Window and wall penetration loss on-site measurements with three methods,'' 12th European Conference on Antennas and Propagation (EuCAP), London, 2018, pp. 1-5.

[39] X. Liao, et al., ``Experimental study of diffuse scattering from typical construction materials over 40-50GHz,'' IEEE Asia-Pacific Conference on Antennas and Propagation (APCAP), Auckland, 2018, pp. 216-218.

[40] Y. Shao, X. Liao and Y. Wang, ``Complex permittivity of typical construction materials over 40–50 GHz,'' IEEE International Symposium on Antennas and Propagation & USNC/URSI National Radio Science Meeting, Boston, MA, 2018, pp. 2003-2004.

[41] J. Zhang, et al., ``Wireless energy efficiency evaluation for buildings under design based on analysis of interference gain,'' IEEE Trans. Veh. Tech., vol. 69, no. 6, pp. 6310-6324, Jun. 2020.

[42] Y. Zhang, et al., ``How friendly are building materials as reflectors to indoor LOS MIMO communications?,'' IEEE Internet Things J., vol. 7, no. 9, pp. 9116-9127, Sept. 2020.

[43] H. Zhao, et al., ``28 GHz millimeter wave cellular communication measurements for reflection and penetration loss in and around buildings in New York city'', Proc. IEEE Int. Conf. Commun. (ICC), 2013, pp. 5163-5167.

[44] Y. Zhang, et al., ``Effects of wall reflection on the per-antenna power distribution of ZF-precoded ULA for indoor mmWave MU-MIMO transmissions,'' IEEE Commun. Lett., accepted for publication, 2020.

[45] J. Zhang, et al., ``Two-ray reflection resolution algorithm for planar material electromagnetic property measurement at the millimeter-wave bands,'' Radio Sci., vol. 55, no. 3, Mar. 2020.

[46] ITU-R, ``Effects of building materials and structures on radiowave propagation above about 100 MHz P series radiowave propagation,'' Recomm. ITU-R P.2040-1, Jul. 2015.

[47] E. Bjornson, et al., “Massive MIMO in sub-6 GHz and mmWave: physical, practical, and use-case differences,” IEEE Wireless Communications, vol. 26, no. 2, pp. 100-108, April 2019.

[48] H. Tian, et al., “Effect level based parameterization method for diffuse scattering models at millimeter-wave frequencies,” IEEE Access, vol. 7, pp. 93286-93293, 2019.

[49] V. Degli-Esposti, et al., "Measurement and Modelling of Scattering From Buildings," in IEEE Transactions on Antennas and Propagation, vol. 55, no. 1, pp. 143-153, Jan. 2007.

[50] Hu, M., Chang, Y., Zeng, T., Yang, X., & Men, A. User grouping with adaptive group number for massive MIMO downlink systems. In 2017 20th International Symposium on Wireless Personal Multimedia Communications (WPMC) (pp. 459-464). IEEE. (2017, December).

[51] Rui, M., Ruo, C., Chaowei, W., & Weidong, W. Downlink transmission scheme for massive MU-MIMO system with reduced CSI. In 2014 4th IEEE International Conference on Network Infrastructure and Digital Content (pp. 322-327). IEEE. (2014, September).

[52] Zeng, T., Chang, Y., Hu, M., & Zhang, Y. CSI-RS based joint grouping and scheduling scheme with limited SRS resources. In 2018 IEEE 29th Annual International Symposium on Personal, Indoor and Mobile Radio Communications (PIMRC) (pp. 1-6). IEEE. (2018, September).

[53] Bahceci, I., Hasan, M., & Cetiner, B. A. Downlink multi-user MIMO transmission for reconfigurable antenna systems. In 2017 IEEE Wireless Communications and Networking Conference (WCNC) (pp. 1-6). IEEE. (2017, March).

[54] H. Q. Ngo, "Cell-free massive MIMO," Encyclopedia of Wireless Networks, pp. 1-6, 2018.

[55] H. Q. Ngo, A. Ashikhmin, H. Yang, E. G. Larsson, and T. L. Marzetta, "Cell-free massive MIMO: Uniformly great service for everyone," in 2015 IEEE 16th International Workshop on Signal Processing Advances in Wireless Communications (SPAWC), 2015.

[56] E. G. Larsson and L. V. der Perre, "Massive MIMO for 5G," IEEE 5GTech Focus, vol. 1, no. 1, 2017.

[57] N. Tawa, T. Kuwabara, Y. Maruta, M. Tanio, and T. Kaneko, "28 GHz Downlink Multi-User MIMO Experimental Verification using 360 Element Digital AAS for 5G Massive MIMO," inProceedings of the 48th European Microwave Conference, 2018

[58] E. Nayebi, A. Ashikhmin, T. L. Marzetta, H. Yang, and B. D. Rao, "Precoding and power optimization in cell-free massive MIMO systems," IEEE Transactions on Wireless Communications, vol. 16, pp. 4445-4459, 2017.

[59] L. D. Nguyen, T. Q. Duong, H. Q. Ngo, and K. Tourki, "Energy efficiency in cell-free massive MIMO with zero-forcing precoding design," IEEE Communications Letters, vol. 21, pp. 1871-1874, 2017.

[60] T. C. Mai, H. Q. Ngo, M. Egan, and T. Q. Duong, "Pilot power control for cell-free massive MIMO," IEEE Transactions on Vehicular Technology, vol. 67, pp. 11264-11268, 2018.

[61] M. Bashar, K. Cumanan, A. G. Burr, M. Debbah, and H. Q. Ngo, "On the uplink max-min SINR of cell-free massive MIMO systems," IEEE Transactions on Wireless Communications, vol. 18, pp. 2021-2036, 2019.

[62] E. Tanghe, W. Joseph, L. Verloock, L. Martens, H. Capoen, K. Herwegen, and W. Vantomme, "The industrial indoor channel: large-scale and temporal fading at 900, 2400, and 5200 MHz," IEEE Transactions on Wireless Communications, vol. 7, no. 7, pp. 2740–2751, jul 2008.

[63] G. Interdonato, E. Björnson, H. Q. Ngo, P. Frenger, and E. G. Larsson, "Ubiquitous cell-free massive MIMO communications," EURASIP Journal on Wireless Communications and Networking, 2019, 197.

[64] https://www.itu.int/dms_pub/itu-r/opb/rep/R-REP-M.2412-2017-PDF-E.pdf

[65] R. C. S. of ITU, "Itu-r m.2412-0: Guidelines for evaluation of radio interface technologies for imt-2020," ITU, Tech. Rep., 2017.